IEEE Access
Multidisciplinary | Rapid Review | Open Access Journal

Received August 10, 2019, accepted August 21, 2019, date of publication August 26, 2019, date of current version September 6, 2019.

Digital Object Identifier 10.1109/ACCESS.2019.2937512

Extremely Optimized DRLSE Method and Its Application to Image Segmentation

DENGWEI WANG
School of Aeronautics and Astronautics, University of Electronic Science and Technology of China, Chengdu 611731, China
Aircraft Swarm Intelligent Sensing and Cooperative Control Key Laboratory of Sichuan Province, Chengdu 611731, China

e-mail: wdengwei@126.com

This work was supported in part by the Fundamental Research Funds for the Central Universities of China under Grant ZYGX2018J079, and in part by the China Scholarship Council (CSC) under Grant 201706075068.

ABSTRACT This paper proposes an extremely optimized distance regularized level set evolution (EO-DRLSE) method for image segmentation applications within the framework of level set method (LSM), which combines various types of local statistical features and adopts an adaptive regularization strategy which specifically serves for zero level set. Firstly, a variable coefficient for the contour length regularization term is designed based on the local normalized entropy, which can adaptively refreshes its value with the change of local disturbance characteristics of the image. Secondly, based on the local fitting means, the constant coefficient of the region term of the original DRLSE model is modified as an adaptive variable with its value changes as the local fitting mean changes. Thirdly, an improved edge stop function is constructed based on the local fitting variances, which enables the evolution process to maintain a considerable evolution speed in the non-target noise interference position without stopping. Obviously, this gives our algorithm a particularly strong noise suppression ability. Fourthly, an additional regularization term that only deals with the zero level curve is added besides the original regularization scheme (the whole level set function (LSF) is regularized). The extended combined regularization strategy further enhances the noise suppression ability and the adaptability to weak edges of the proposed model. Fifthly, two implementation strategies named morphological snakes and significant target detection mechanism are used to ensure the rapidity and automation of the evolution process. The extensive experiments on a large variety of synthetic and real images show that the proposed algorithm achieves excellent performance in terms of accuracy of segmentation results, rapidity of evolution process, robustness against noise, adaptability to weak target edges. In addition, the factors that can have a key impact on segmentation performance are also analyzed in depth.

INDEX TERMS DRLSE, morphological snakes, salient target detection, level set, image segmentation.

I. INTRODUCTION

In computer vision, image segmentation is the process of partitioning a digital image into multiple segments. The goal of segmentation is to simplify and/or change the representation of an image into something that is more meaningful and easier to analyze. Image segmentation is typically used to locate objects and boundaries (lines, curves, etc.) in images. More precisely, image segmentation is the process of assigning a label to every pixel in an image such that pixels with the same label share certain characteristics. In the field of image segmentation, there are two forms of label: one is binary form (0 or 1); the other is multi-valued form, which takes continuous values in [0, 1], and we call it soft segmentation or image matting [1]. The result of image segmentation is a set of segments that collectively cover the entire image, or a set of contours extracted from the image. Each of the pixels in a region is similar with respect to some characteristic or computed property, such as color, intensity, or texture. Adjacent regions are significantly different with respect to the same characteristic(s). Among various types of image segmentation theories, the level set methods (LSMs) are widely used because they are capable of outputting closed and smooth target contours and can naturally handle topology changes. The LSMs are a conceptual framework for using level sets as a tool for numerical analysis of surfaces and shapes [2].

The associate editor coordinating the review of this article and approving it for publication was Md. Asikuzzaman.

The advantage of the LSM is that one can perform numerical computations involving curves and surfaces on a fixed Cartesian grid without having to parameterize these objects (this is called the Eulerian approach). Also, the LSM makes it very easy to follow shapes that change topology, for example, when a shape splits in two, develops holes, or the reverse of these operations. All these make the LSM a great tool for modeling time-varying objects, like inflation of an airbag, or a drop of oil floating in water.

According to the properties of the image features used in the construction of their energy functionals by the LSMs for image segmentation applications, we can classify them into the following two categories: edge-based methods [3]–[10] and region-based methods [11]–[19].

Edge-based methods usually rely on the gradient features of the image to construct their main external driving forces. Such methods can achieve high-quality segmentation results when the target's gradient amplitude is relatively obvious and the degree of noise interference in the background is low. However, once the noise in the image becomes noticeable or the edge region of the target is very blurred (the corresponding gradient amplitude is small), the evolution of such models is likely to present the following problems: trapping into local minima (being pulled to the wrong background interference position), edge leakage (losing the edge elements belonging to the target), sensitive to noise (being easily affected by noise). For example, as a typical representative of edge-based methods, the geodesic active contours (GAC) model proposed by Caselles *et al.* [3] has achieved unprecedented success in the task of high quality image data segmentation. However, when the noise in the image becomes non-negligible or the gradient magnitude of the target is not obvious, its segmentation accuracy will drop sharply, and the aforementioned problems will also occur. Li *et al.* [4] proposed a segmentation framework called distance regularized level set evolution (DRLSE). The distance regularization effect eliminates the need for reinitialization and thereby avoids its induced numerical errors. The DRLSE framework does output good segmentation results on some high-quality images. However, it has two obvious drawbacks: one is that the speed of curve evolution cannot be adaptively changed with the change of local image characteristics, and the other is that its segmentation result is highly sensitive to noise. By integrating the adaptive perturbation thought into the edge-based active contour framework, Yu *et al.* [10] designed an active contour model for medical image segmentation applications. This model does output good segmentation results on high quality medical images. However, when the edge feature of the image is not very obvious (weak edge phenomenon is very common in medical image data), the model is difficult to output valuable segmentation results.

Region-based methods usually construct their external driving forces from the statistical information of the inner and outer regions (global or local) separated by active contours, and the common statistical objects have intensity, color, texture, and transform domain features, etc. Compared with edge-based methods, such methods do have significant improvements in terms of weak edge capture, background interference suppression, robustness to noise, etc. However, such methods also have their own mechanical defects, namely, they sometimes cannot accurately locate the true target edge position. For example, based on the mean intensity measurement of the region, the C-V model proposed by Chan and Vese [11] can globally fit the internal and external intensity means of the active contour. When the integral effect of the difference between the discrete pixels and the statistical means reaches the optimal value, the curve can converge to the desired position of the model. Applying it to images without obvious edges or even without edges can usually achieve obtain satisfactory segmentation performance. However, in many cases, its edge positioning accuracy is not high. By using the Gaussian distribution with adaptive mean and variance as the describing tool of image local region, Wang *et al.* [15] constructed a LSM called local Gaussian distribution fitting (LGDF) energy model for image segmentation. Zhang et al. [16] presented an LSM named local image fitting (LIF) energy model whose energy functional is defined by minimizing the difference between the fitted image and the original image. Ding et al. [17] proposed an active contour model which integrates the optimized Laplacian of Gaussian energy term with the region-scalable fitting (RSF-LoG) energy term which makes use of local region information to drive the curve towards the boundaries. By computing average image intensities locally before the evolution of curve, Ding et al. [18] presented an active contour model using local pre-fitting energy (LPFE) for image segmentation. By fully utilizing the spatial constraints of neighborhood pixels, Yu *et al.* [19] proposed a regional active contour model for image segmentation under the framework of local patch similarity measure. In summary, by localizing the statistical range of image attributes, the aforementioned five local region information-driven LSMs have achieved good segmentation on most images, but these four methods have the following drawbacks: When constructing their local statistical information elements, there is no special consideration for noise. Therefore, noise interference in the local area is very easy to break the balance of local statistical information, making the power from noise components easily become the dominant force in the local window. In addition, these five models also lack internal mechanisms that provide safeguards for weak edges capture.

In order to overcome the problems mentioned above, we construct an optimized image segmentation framework based on the DRLSE model. Firstly, based on the local normalized entropy, we design a variable coefficient for the contour length regularization term of the original DRLSE model, which can vary with the apparent properties of the image region (the smooth region without the target or the undulating region where the target is located). Specifically, in the smooth region, the value of the variable coefficient is relatively small (corresponding to strong regularization) to reduce the probability of the evolution process falling into

the local minimum, while in the region adjacent to the target boundary, the value of the variable coefficient is relatively large (corresponding to weak regularization) to reduce the loss of image details. Secondly, based on the local fitting means, we modify the constant coefficient of the regional term (weighted area term used to accelerate the evolution process) in the original DRLSE model as an adaptive variable with its value changes as the local fitting mean changes. Compared with the original constant coefficient, the rationality of the adaptive coefficient is greatly improved. Thirdly, in order to improve the robustness of the edge stopping function in the original DRLSE model to noise, we construct an optimized edge stop function based on the local fitting variances. The new edge stop function can still maintain an appropriate evolution speed at non-target noise locations, namely, it can effectively suppress noise interference. Fourthly, besides the original regularization scheme (the whole LSF is regularized), we also add an additional regularization term which only deals with the zero level curve specially. The extended compound regularization system further enhances the noise suppression ability and the adaptability to weak edges of the proposed model. Fifthly, two implementation strategies are used to improve the execution efficiency of the evolution process. The first is a numerical scheme called morphological snakes [20], which does not need to solve partial differential equations and can greatly speed up the evolution process. The second is salient target detection mechanism-based curve initialization scheme, which not only realize automatic initialization, but also reduce the subjective and purposeful influence of artificial initialization.

The main contributions and innovations of this paper are summarized as follows:

(1) *We construct a coefficient that can adaptively adjust the regularization strength for the length term.* The variable coefficient is based on the local normalized entropy, and its value can be adaptively changed with the local disturbance characteristics (which can be described by local entropy) of the image. Its change law is highly consistent with the evolution trend of the regularization strength needed by the image.

(2) *We design a coefficient for the regional term that can adaptively adjust the speed of evolution.* Its value can be adjusted dynamically with the change of local fitting means, and its numerical change law reflects exactly the need for speed in the evolution process. In other words, in a smooth region that needs to move forward quickly, its value happens to be large, on the contrary, it happens to be small in the neighborhood of edge where the speed needs to be slowed down.

(3) *We design an edge stop function with strong noise suppression ability:* This local fitting variances-guided new edge stop function has a considerable evolution speed even at non-target noise locations. In other words, our edge stop function can effectively suppress noise, which is an ability that the original DRLSE model does not have.

(4) *We construct an additional adaptive regularization term with strong noise suppression ability and weak edge adaptability that specifically serves for the zero level set:* The adaptive regularization here forms a strong extension to the level set regularization scheme of the original DRLSE model, and the anti-noise ability and weak edge adaptability of the proposed method are further enhanced.

(5) *The morphological snakes and salient target detection mechanism are combined to improve the execution efficiency of the evolution process:* In order to overcome the inherent structural defects of the traditional finite difference scheme and improve the automation of the initialization process, in the implementation stage, we adopt two sets of strategies. One is a fast numerical solution based on morphological snakes, which replaces the floating point differential operations required by the traditional partial differential equations by means of special integer morphological operations. The other is an automatic initialization scheme based on salient target detection mechanism, which makes the proposed algorithm fully automated. This kind of processing is extremely valuable in some applications where human participation is not allowed.

The remainder of this paper is organized as follows: In section II, we briefly review the original DRLSE model and point out its problems. Section III discusses the energy functional construction process of the proposed method in detail. Then, the implementation strategies for the proposed model are presented in section IV. Section V validates the proposed model by extensive comparison experiments and discussions on a variety of images. Finally, some conclusive remarks are provided in section VI.

II. A SIMPLE REVIEW OF THE ORIGINAL DRLSE MODEL

By adding a distance regularization term to the traditional energy function, the DRLSE model effectively overcomes the time-consuming re-initialization problem in the evolution of the traditional level set. Since the distance regularization term in the DRLSE model can automatically correct the deviation between the current level set function and the signed distance function, the traditional time-consuming re-initialization operation is completely unnecessary. In the level set formulation, the contour C which separates the image into a series of sub-regions can be represented as the zero level set of a Lipschitz function $\phi(x, y) : \Omega \rightarrow R$, such that $\phi(x, y) > 0$ if the point (x, y) is inside C, $\phi(x, y) < 0$ if (x, y) is outside C, and $\phi(x, y) = 0$ if (x, y) is on C. With the level set representation, the energy functional of the DRLSE model can be defined as follows:

$$\begin{aligned} E(\phi) &= \mu R_p(\phi) + \lambda L_g(\phi) + \alpha A_g(\phi) \\ &= \mu \int_\Omega p(|\nabla\phi|)\, dx + \lambda \int_\Omega g\delta_\varepsilon(\phi)\, |\nabla\phi|\, dx \\ &\quad + \alpha \int_\Omega g H_\varepsilon(-\phi)\, dx \end{aligned} \tag{1}$$

where μ and λ are positive control constants, α is a control constant in the range of real numbers, ϕ is the LSF,

$R_p(\phi)$ is the internal energy term used to eliminate the re-initialization operation, the length regularization term $L_g(\phi)$ and the region (area) regularization term $A_g(\phi)$ together constitute the external energy term of the DRLSE model. The role of the length regularization term $L_g(\phi)$ is to drive the zero level set to evolve towards the target edge, while the purpose of the region regularization term $A_g(\phi)$ is to accelerate the evolution rate of the LSF, g is the edge stop function, ∇ is the gradient operator, $p(\cdot)$ is the potential function, $\delta_\varepsilon(\phi)$ and $H_\varepsilon(\phi)$ are the regularized Dirac delta function and the regularized Heaviside function, respectively.

The integral functions g involved in Eq. (1) is defined as follows:

$$g = \frac{1}{1 + |\nabla G_\sigma * I|^2} \tag{2}$$

where G_σ is a Gaussian kernel with a standard deviation. The convolution in (2) is used to smooth the image to reduce the noise. This function usually takes smaller values at object boundaries than at other locations.

The definition of the double-well potential function $p(\cdot)$ used in Eq. (1) is as follows:

$$p(|\nabla\phi|) = \begin{cases} \frac{1}{(2\pi)^2}\left(1 - \cos\left(2\pi|\nabla\phi|\right)\right), & if \ |\nabla\phi| \le 1 \\ \frac{1}{2}\left(|\nabla\phi| - 1\right)^2, & if \ |\nabla\phi| \ge 1 \end{cases} \tag{3}$$

The definitions of the two functions $H_\varepsilon(\phi)$ and $\delta_\varepsilon(\phi)$ of Eq. (1) are as follows:

$$\delta_\varepsilon(x) = \begin{cases} \frac{1}{2\varepsilon}\left[1 + \cos\left(\frac{\pi x}{\varepsilon}\right)\right], & |x| \le \varepsilon \\ 0, & |x| > \varepsilon \end{cases} \tag{4}$$

$$H_\varepsilon(x) = \begin{cases} \left(1 + x/\varepsilon + 1/\pi \times \sin\left(\pi x/\varepsilon\right)\right)/2, & |x| \le \varepsilon \\ 1, & x > \varepsilon \\ 0, & x < -\varepsilon \end{cases} \tag{5}$$

where ε is a control parameter that can affect the properties of $\delta_\varepsilon(\phi)$ and $H_\varepsilon(\phi)$. For example, for $\delta_\varepsilon(\phi)$, a bigger ε will cause a broader profile, which will expand the capture scope but decrease the accuracy of the final contour.

Since the energy functional uses the gradient amplitude-driven edge stop function, the DRLSE model can effectively segment the image with sharp edge characteristics. However, the model has the following problems: ① Its edge stop function simply depends on the gradient of the image, so it is easy to cross the weak target edges and cause edge leakage phenomenon; ② It lacks an internal mechanism that can effectively suppress noise, so the segmentation results of this model are extremely sensitive to noise; ③ Its numerical implementation process needs to solve partial differential equations and relies on the traditional finite difference scheme, thus the time cost of the evolution process is very large; ④ The existence of multiple constant coefficients makes its evolution process lack of adaptability; ⑤ The segmentation results are highly correlated with initialization, so the automatic initialization strategy based on third-party algorithm is not applicable to this model; ⑥ Its regularization operation takes the whole LSF as its execution object, and does not specifically consider the zero level curve which is related to the success or failure of target acquisition.

III. THE PROPOSED MODEL

A. LOCAL NORMALIZED ENTROPY-GUIDED ADAPTIVE COEFFICIENT FOR THE LENGTH REGULARIZATION TERM

In the process of LSE, we often need to make appropriate corrections to the length of the active contour, i.e., regularization, so that the active contour can maintain sufficient smoothness. The length regularization term of the original DRLSE model has a constant modulation coefficient λ, which has many defects (the analysis process is shown in the following section). In this section, we will construct a novel adaptive coefficient that varies with the change of image coordinates for the length regularization term of the original DRLSE model by applying the concept of entropy in the field of image segmentation. In this paper, we actually use the local normalized entropy, which is defined as follows:

$$E(x, \Omega_x) = \frac{\int_{\Omega_x} p(y, \Omega_x) \ln\left(p(y, \Omega_x)\right) dy}{\max\limits_{x \in \Omega}\left(\int_{\Omega_x} p(y, \Omega_x) \ln\left(p(y, \Omega_x)\right) dy\right)} \tag{6}$$

As we all known, entropy is a kind of statistics that can effectively describe the degree of information disorder. It has the following features: when the degree of information disorder is low (the data is relatively smooth), the value of entropy is small; on the contrary, when the degree of data disorder is high (the test data contains edge and other types of jumps), the value of entropy is large. According to the above features, we can easily conclude that the normalized entropy is close to 0 when the pixel x is in the smooth image region, while when the pixel x is located in the adjacent region of target edge, the value of normalized entropy will be close to 1.

When we assume that the value of g in the original DRLSE model is 1, the second term in the DRLSE model will be simplified to $\lambda\delta_\varepsilon(\phi)\, div\left(\frac{\nabla\phi}{|\nabla\phi|}\right)$, where $div\left(\frac{\nabla\phi}{|\nabla\phi|}\right)$ is the curvature metric of the curve. Now, let's continue to assume that the value of the second term of DRLSE is fixed. At this time, the curvature $div\left(\frac{\nabla\phi}{|\nabla\phi|}\right)$ will have an inverse proportional relationship with the coefficient λ. Under the support of the inverse relationship described above, we can observe the following phenomenon: the larger coefficient λ will correspond to a smaller curvature. In this case, the regularization and smoothing effects applied to the LSF are very weak. When the value of the coefficient λ is small, the value of the curvature will become very large, and the smoothing and regularization effects are strong at this time.

Due to the regularization and smoothing effects on the length of the curve, some details of the image may be lost to some extent. In the case where the image contains noise interference, if the details of the image are lost too seriously,

it is very likely that the active contour will cross the target edge. Therefore, we need a larger coefficient value to prevent such phenomena. However, larger coefficient values may in turn cause the active contour to fall into local minima (false target edges) in the smooth region of the image. When the coefficient is small, another kind of contradiction will appear. In a word, it is difficult to get ideal modulation effect based on edge regularization term with constant coefficient λ. In summary, the ideal coefficient λ should have the following characteristics: in a smooth region, the value of the coefficient λ should be as small as possible to reduce the probability that the evolution process falls into a local minimum; while in the region near the target edge, the coefficient should be as large as possible to reduce the loss of image details. In order to meet the aforementioned requirements, based on the normalized entropy shown in Eq. (6), we construct an adaptive coefficient with the following expression:

$$\lambda_{length} = mE\left(x, \Omega_x\right) + n \tag{7}$$

where m is a positive constant and n is a small correction constant which is intentionally introduced to avoid the coefficient prematurely approaching zero. Since the value range of $E\left(x, \Omega_x\right)$ is $[0, 1]$, the value of λ_{length} will be limited to range $[n, m+n]$. When the pixel x is located in the smooth region, the coefficient will approach n. The reason is that the local entropy is close to 0, which provides a strong guarantee for the strong regularization ability needed in the smooth region. On the contrary, when the pixel x is near the edge, the coefficient will approach $m+n$, which provides a strong support for the weak regularization ability needed in the evolution process.

B. LOCAL FITTING MEANS-GUIDED ADAPTIVE REGIONAL COEFFICIENT

The role of the regional energy term of the DRLSE framework is to accelerate the evolution of the LSF, which is especially necessary when the initial curve is away from the target to be segmented.

In the original DRLSE model, the coefficient of the regional term is set to a constant, which always remains unchanged during the evolution of the LSF. A large coefficient value allows the active contour to evolve rapidly toward the target, but there may be edge leak problem, i.e., there is no stop where it should stop (target edge); on the contrary, a small coefficient value can ensure that the active contour stays on the target edge steadily, but it may make the evolution process dock on other pseudo-edges synchronously, i.e., stop where it should not stop (local minima such as pseudo-edges), so it is difficult to determine a suitable constant coefficient by experience alone.

In order to effectively solve the above problems, we construct the following adaptive coefficient based on the local fitting means of the image:

$$v_{LFM}\left(x\right) = ae^{-b\left|f_{in}(x) - f_{out}(x)\right|} + c \tag{8}$$

where a and b are positive linear and nonlinear constants respectively, c is a small positive constant to avoid $v_{LFM}\left(x\right)$ prematurely going to zero, $f_{in}\left(x\right)$ and $f_{out}\left(x\right)$ are the local fitting means of the inner and outer regions with the active contour as the separating curve and the statistical range is the Gaussian kernel window centered at pixel x, their definitions are as follows:

$$f_{in}\left(x\right) = \frac{\int_{\Omega} G_{\sigma}\left(x-y\right)\left[I\left(y\right)H\left(\phi\left(y\right)\right)\right]dy}{\int_{\Omega} G_{\sigma}\left(x-y\right)H\left(\phi\left(y\right)\right)dy} \tag{9}$$

$$f_{out}\left(x\right) = \frac{\int_{\Omega} G_{\sigma}\left(x-y\right)\left[I\left(y\right)\left(1-H\left(\phi\left(y\right)\right)\right)\right]dy}{\int_{\Omega} G_{\sigma}\left(x-y\right)\left(1-H\left(\phi\left(y\right)\right)\right)dy} \tag{10}$$

where $G_{\sigma}\left(\cdot\right)$ is the Gaussian kernel function with scale factor equal to σ.

The coefficient $v_{LFM}\left(x\right)$ shown in Eq. (8) has the following properties: ① when the pixel being counted is in a smooth region, the value of $\left|f_{in}\left(x\right) - f_{out}\left(x\right)\right|$ is small, and correspondingly, the coefficient $v_{LFM}\left(x\right)$ has a relatively large value; ② when the pixel under consideration is adjacent to target edge, the values of $f_{in}\left(x\right)$ and $f_{out}\left(x\right)$ will show a large difference. Therefore, the value of $\left|f_{in}\left(x\right) - f_{out}\left(x\right)\right|$ is relatively large, and correspondingly, the coefficient $v_{LFM}\left(x\right)$ has a small value. This kind of numerical changing law is exactly what we need. It intuitively means that the evolution process has a relatively fast advancing speed in smooth regions, thus ensuring that the active contour moves toward the target region quickly. When approaching the target edges, the speed of the evolution process will gradually decrease, which ensures that the target will not be lost and will not stop prematurely.

C. LOCAL FITTING VARIANCES-GUIDED EDGE STOP FUNCTION

The role of the edge stop term shown in the DRLSE framework is to make the evolution properly docked at the true target edge. The edge stop terms are usually constructed based on some statistical properties of the image and there is no uniform form of their function structure. Different edge stop functions tend to produce different segmentation results. The original DRLSE framework relies on the gradient information of the image when constructing its edge stop function. It is well known that the edge stop function with the gradient value of the image as the single-mode information source is highly susceptible to noise interference, which often causes the evolution process to stop at the noise point incorrectly. In order to make the edge stop function not be erroneously pulled by the noise information to the false target position, we construct a new edge stop function with the following expression based on the local fitting variance of the image:

$$g_{LFV}\left(x\right) = \frac{1}{1 + d\left(x\right) \Big/ \left(\sigma_{in}^2\left(x\right) + \sigma_{out}^2\left(x\right) + 1\right)} \tag{11}$$

where $d\left(\cdot\right)$ is the gradient function of the image, $\sigma_{in}^2\left(x\right)$ and $\sigma_{out}^2\left(x\right)$ are the local fitting variances of the inner and outer regions with the active contour as the separating

curve and the statistical range is the Gaussian kernel window centered at pixel x. Their mathematical expressions are as follows:

$$\sigma_{in}^2(x) = \frac{\int_\Omega G_\sigma(x-y)\left[(I(y)-f_{in}(x))^2 H(\phi(y))\right]dy}{\int_\Omega G_\sigma(x-y) H(\phi(y))\,dy} \tag{12}$$

$$\sigma_{out}^2(x) = \frac{\int_\Omega G_\sigma(x-y)\left[(I(y)-f_{\text{out}}(x))^2 H(\phi(y))\right]dy}{\int_\Omega G_\sigma(x-y) H(\phi(y))\,dy} \tag{13}$$

The improved edge stop function $g_{LFV}(x)$ has the following properties: ① when the pixel x to be inspected is located in a smooth region and there is no noise interference in its neighborhood, both $d(x)$ and $\left(\sigma_{in}^2(x)+\sigma_{out}^2(x)\right)$ have very small values, and the edge stop function at this time satisfies the condition $g_{LFV}(x) \to 1$; ② when the pixel x is located in a smooth region and the neighborhood contains noise interference, both $d(x)$ and $\left(\sigma_{in}^2(x)+\sigma_{out}^2(x)\right)$ will present relatively large values, which causes $g_{LFV}(x)$ to get a positive value that is not close to zero; ③ when the sampling pixel x is adjacent to the edge of the target, the value of $d(x)$ is very large, while and the value of $\left(\sigma_{in}^2(x)+\sigma_{out}^2(x)\right)$ is very small, and the edge stop function at this time will satisfy the condition $g_{LFV}(x) \to 0$. The traditional edge stop functions also have attributes ① and ③, while the attribute ② is unique to the new edge stop function g_{LFV}, which makes the proposed model robust to noise interference.

D. ADAPTIVE REGULARIZATION TERM

The regularization operation of the original DRLSE model takes the whole LSF as its execution object, and does not give special consideration to the zero level curve related to the success or failure of target acquisition. In order to overcome this defect and further improve the smoothness of the LSE process, we added an adaptive regularization constraint that is directly applied to the zero level set in addition to the original regularization scheme, the effect of which is to reduce the influence of noise and ensure that the active contour does not pass through the weak object boundaries. In order to solve the problem of regularization of zero level curve, Zhou and Mu [21] proposed an efficient regularization scheme based on weighted Dirichlet integral. Although this method has achieved good results, its constant exponent gives it the following problems: cannot effectively reflect the local characteristics of the image, therefore, the regularization scheme cannot let the exponent automatically adapt to the image data. In order to enhance the adaptability of the constraint to the local image information, we propose the following weighted Dirichlet integral regularization with variable exponent:

$$R_{zero}(\phi) = \iint_\Omega \delta(\phi)\frac{|\nabla\phi|^{f(|\nabla(G_\sigma * I)|)}}{f(|\nabla(G_\sigma * I)|)}dxdy \tag{14}$$

where "$G_\sigma * I$" is the convolution operation between the image I and the Gaussian filter kernel G_σ (whose standard deviation is σ), "∇" is a gradient operator, the exponent $f(n)$ is a strictly monotone function and has the following limiting properties: ① $\lim_{n\to 0} f(n) = 1$; ② $\lim_{n\to+\infty} f(n) = 1.5$. By matching these two features, we can construct the following simple function:

$$f(n) = 1.5 - \frac{1}{n+2} \tag{15}$$

Below we briefly analyze the macroscopic properties of the function $R_{zero}(\phi)$:

① When $f(|\nabla(G_\sigma * I)|)$ equals to 1, $R_{zero}(\phi)$ will degenerate to the following simple form: $R_{zero}(\phi) = \iint_\Omega \delta(\phi)|\nabla\phi|dxdy$. By comparing it with the C-V model, we find that this degenerate form is the curve length constraint used in the C-V model, which calculates the length of the zero curve of the LSF ϕ.

② When $f(|\nabla(G_\sigma * I)|)$ is a constant F greater than 1, $R_{zero}(\phi)$ will be simplified as a geometric constraint for zero level curve used in [20].

For most images, the intensity value of the same foreground area is not strictly uniform, that is to say, different local areas within the foreground range have different local characteristics. Under this generality, if the above exponent $f(\cdot)$ is set as a constant, the local characteristics of the image cannot be correctly reflected, in other words, the exponent $f(\cdot)$ cannot automatically match the image data. Therefore, it is very unreasonable to set the exponent $f(\cdot)$ constant. In view of this, we take a different approach. In our framework, the exponent $f(\cdot)$ is directly related to the local intensity information of the image. Our approach ensures that weak regularization ($f(|\nabla(G_\sigma * I)|) \approx 1$) is performed within regions with almost constant intensity values (the gradient value of the image is almost zero), as a result, it can effectively avoid the problem of the disappearance of weak boundaries. In contrast, in other areas, it will take a strong regularization operation to force the removal of false contours. Therefore, the existence of variable exponent $f(\cdot)$ makes our regularization scheme adaptively choose between weak regularization and strong regularization.

E. EXTREMELY OPTIMIZED AND CUSTOMIZED DRLSE MODEL

By introducing the elements from sub-sections III. A to III. D into the original DRLSE framework, we constructed a deeply optimized and customized DRLSE model with the following definition:

$$\begin{aligned} E^{total}&\left(\phi(x), \lambda_{length}(x), \nu_{LFM}(x), g_{LFV}(x)\right) \\ &= \mu\left(R_p(\phi) + R_{zero}(\phi)\right) \\ &\quad + \lambda_{length}(x)\int_\Omega g_{LFV}(x)\,\delta_\varepsilon(\phi(x))\,|\nabla\phi(x)|\,dx \\ &\quad + \nu_{LFM}(x)\int_\Omega g_{LFV}(x)\,H_\varepsilon(-\phi(x))\,dx \end{aligned} \tag{16}$$

What needs to be specifically stated here is that the support domain of Eq. (4) is $[-\varepsilon, \varepsilon]$, which determines that the control ability of the evolution process is local. In order to

expand its scope of action, this paper uses the following new regularized Dirac function $\delta_\varepsilon^{new}(\cdot)$ to replace the $\delta_\varepsilon(\cdot)$ in Eq. (16):

$$\delta_\varepsilon^{new}(x) = \frac{1}{\pi}\frac{\varepsilon}{\varepsilon^2 + x^2}, \quad x \in R \tag{17}$$

Since the support domain of function $\delta_\varepsilon^{new}(x)$ is $(-\infty, +\infty)$, Eq. (16) will act on the entire LSF, so that the global minimum of the energy functional can be obtained, which further improves the ability of the zero level set to detect multi-layer contours, and the ability to capture deeply concave regions and multiple target boundaries.

Keeping the optimized coefficients and the edge stop function fixed, and minimizing the energy functional $E^{total}\left(\phi(x), \lambda_{length}(x), \nu_{LFM}(x), g_{LFV}(x)\right)$ with respect to ϕ, the gradient flow equation corresponding to Eq. (16) can be obtained as:

$$\begin{aligned}\frac{\partial\phi}{\partial t} = -\frac{\partial E^{total}}{\partial\phi} &= \mu div\left(d_p\left(|\nabla\phi|\right)\nabla\phi\right) \\ &+\mu\delta_\varepsilon^{new}(\phi)\, div\left(|\nabla\phi|^{f(|\nabla(G_\sigma * I)|)-2}\nabla\phi\right) \\ &-\mu\left(\frac{1}{f\left(|\nabla G_\sigma * I|\right)} - 1\right)\delta_\varepsilon^{'}|\nabla\phi|^{f(|\nabla(G_\sigma * I)|)} \\ &+\lambda_{length}\delta_\varepsilon^{new}(\phi)\, div\left(g_{LFV}\frac{\nabla\phi}{|\nabla\phi|}\right) + \nu_{LFM}\, g_{LFV}\,\delta_\varepsilon^{new}(\phi)\end{aligned} \tag{18}$$

where $\delta_\varepsilon^{'}$ is the partial derivative of $\delta_\varepsilon^{new}(\phi)$ with respect to ϕ, and $d_p(\cdot)$ is a function defined as $d_p(s) = p^{'}(s)\Big/ s$. The first three terms are a whole, where the first one is to regularize the whole LSF to improve the smoothness of the evolutionary surface, and the purpose of the second and third terms is to perform a regularization operation on the zero level set of the LSF to minimize the influence of noise interference and prevent the active contours from crossing the weak target edge. Under the joint action of the adaptive coefficients λ_{length} and ν_{LFM} and the modified edge stop function g_{LFV}, the third and fourth terms show strong robustness to noise interference, which can ensure that the evolution curve moves forward rapidly in a smooth region and stops steadily at the real target edge. This has achieved the overall goal: go forward where it should go, and stop where it should stop. Based on Eq. (18), we can realize the iterative updating of the LSF ϕ, and then realize the dynamic evolution of the curve.

IV. IMPLEMENTATION STRATEGIES

A. MORPHOLOGICAL SNAKES-BASED NUMERICAL IMPLEMENTATION

After obtaining the gradient descent equation of the level set segmentation model, the traditional methods usually use the finite difference method to numerically solve it. This kind of algorithm is simple, easy to understand, intuitive, and easy to implement by computer programming. However, such numerical implementation methods have obvious drawbacks, i.e., their time consumption is often too high to meet the high requirements of evolution speed in some special applications. In order to improve the evolution speed of level set equation, the researchers have designed a variety of methods. For example, [22] uses AOS strategy to solve the divergence term efficiently. Reference [23] makes full use of the characteristic that algebraic multigrid can support a large time step and achieves high-speed numerical implementation under its guidance. Based on the loose time step limitation and parallelization characteristics of the lattice Boltzmann method, a fast numerical solution strategy is designed in [24]. Although these methods have achieved good acceleration results, they are all processed within the framework of floating-point number. For the hardware implementation process of the back-end of a complete visual information processing system, there are different degrees of conversion errors. To overcome this problem, Marquez-Neila *et al.* [20] proposed the idea of morphological snakes. The morphological snakes use morphological operators (such as dilation or erosion) over a binary array instead of solving PDEs over a floating point array, which is the standard approach for active contours. This makes morphological snakes faster and numerically more stable than their traditional counterpart. In view of the excellent characteristics of the morphological snakes in terms of numerical implementation, this paper uses the morphological snakes as our numerical solution scheme.

B. SALIENT TARGET DETECTION MECHANISM-BASED AUTOMATIC CURVE INITIALIZATION

Since the evolution equation of the level set is carried out in the form of iterations in the concrete execution, we need to set an initial value for the LSF so that our time iteration process has a reference point. The setting methods of the initial value are usually divided into the following two forms: ① Man-made type. For example, a curve is specified by hand-drawn (by sliding the mouse over the image area to complete the interactive design of the curve) or by parameterizing (giving all the associated parameters of the curve), and then the signed distance function corresponding to this curve is taken as the initial value of the level set; ② Algorithm automatically generated type. For example, the third-party pre-segmentation algorithm is used to output the rough foreground region of the image, and then the contour of the foreground region is extracted and taken as our initial curve. Finally, the signed distance function corresponding to this curve is taken as the initial value of the LSF. Under different application scenarios, we are free to use these two types of initial curve setting strategies, their convenience is no doubt, but their respective shortcomings are obvious: The shortcomings of the first approach are people's strong subjectivity, so it usually unconsciously places the initial curve within the neighborhood of the target of interest, as a result, for the execution process, it is impossible to make an objective evaluation of the overall performance of the level set segmentation algorithm; The shortcomings of the second approach are the output of the pre-segmentation algorithm cannot be predicted, when the pre-segmentation effect is poor, the corresponding initial curve must be very disturbing,

there is no doubt that additional interference is added to our level set segmentation task.

It is true that the targets we intend to segment usually have some form of saliency, therefore, we may achieve a pre-detection of the target region through a salient target detection mechanism, and the outer contour of the output is taken as our initial curve.

FIGURE 1 shows the performance of some classic salient target detection algorithms on several sample images (the experimental results section also uses this set of images), where the first and last columns are input images and ground truth, respectively, and the second to the sixth rows are the saliency maps by using the context-aware (CA) algorithm [25], region covariances-based (COV) algorithm [26], frequency tuned (FT) algorithm [27], graph-based (GB) algorithm [28] and spectral residual (SR) algorithm [29] respectively. In the saliency map, the greater the gray value of these results, the greater the significance of the corresponding position in the input image, and vice versa.

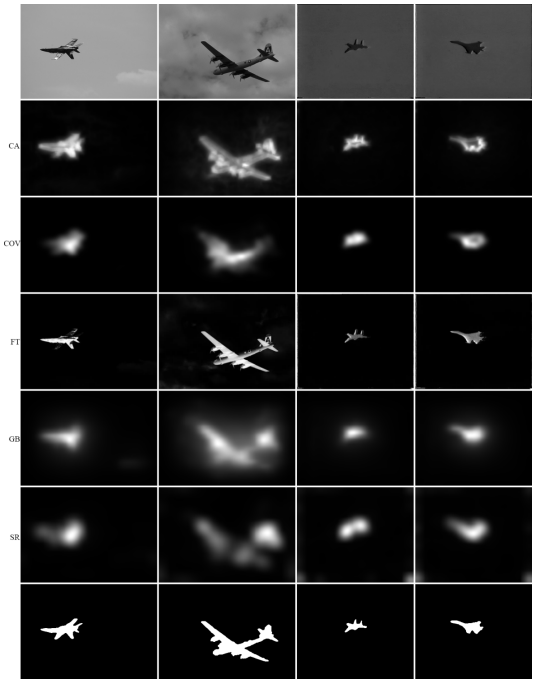

FIGURE 1. The comparison results of different salient target detection algorithms.

From the saliency target output results shown in FIGURE 1, we find that the GB model outputs the optimal saliency map, the reason is that its results have the following two characteristics: ① The pixels in the background region are less salient; ② The pixels in the target region typically have a higher saliency value. In view of this, in the experimental part of this paper, we choose the GB model to achieve the detection of salient targets. In addition, we also found a common phenomenon that the output of a significant target detection algorithm is usually a non-binarized image with a suspected target region, it can't directly give the external contour of the suspected target region, thus we need to further segment the output of the salient detection algorithm in order to get the initial curve of the level set.

Because the output of the salient target detection algorithm has a high degree of fuzzy characteristics, the external contour of the suspected target region is not obvious, therefore, the traditional threshold segmentation algorithms cannot get the ideal segmentation results on this kind of images. However, the CV model based on the theory of level set theory has excellent segmentation performance for such edgeless images. Therefore, this paper uses the CV model to segment the suspected target regions of the salient target detection algorithms.

FIGURE 2 shows the segmentation results of the CV model on the saliency map shown in the second column of FIGURE 1, in order to demonstrate the initialization performance of this processing mode, the final contour curve is superimposed on the original input image shown in FIGURE 1. In initializing the LSE of the CV model, we take the simplest way to draw a rectangle directly above the image, which is 5 pixels from each edge of the input image.

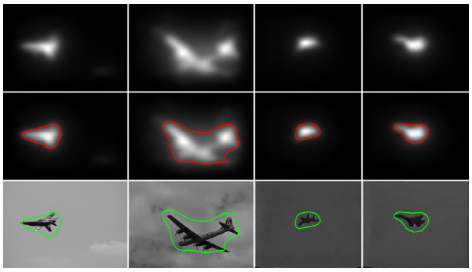

FIGURE 2. Examples of the initial curve determination based on the salient target detection mechanism. The first row: Saliency maps. The middle row: The convergence results of the CV model. The third row: The visual effects after the contour curve is superimposed on the original image.

C. ALGORITHM STEPS

The detailed execution steps of the proposed algorithm are summarized in Algorithm 1.

V. EXPERIMENTAL RESULTS AND DISCUSSIONS

In this section, we shall validate (corresponding to sub-section V. A) the performance of the proposed method on a variety of test images, and give a detailed analysis (corresponding to sub-section V. B) for several key factors that influence the experimental results. All experiments are implemented by Matlab R2012a on a computer with Intel Core i7 2.3GHz CPU, 8G RAM, and Windows 7 operating system. For the control parameters involved in the proposed model, the general principles for setting their values are as follows: The linear constant a in Eq. (8) can be set relatively large to ensure that the evolution process can advance at a higher speed in the smooth region, and it is empirically set to 6 in all experiments. For the parameter b in Eq. (8), since its value will have a slight effect on the sensitivity of the evolution

Algorithm 1 Extremely Optimized DRLSE Model

(I) Automatically initialize the LSE process using the salient target detection mechanism described in section IV. B;
(II) Set relevant control and attribute parameters, including m, n, a, b, c, Δt, μ, σ and ε;
(III) Iteratively update the values of $f_{in}(\cdot)$, $f_{out}(\cdot)$, $\sigma_{in}^2(\cdot)$ and $\sigma_{out}^2(\cdot)$ according to equations (9), (10), (12) and (13) respectively;
(IV) Update the values of λ_{length}, $\nu_{LFM}(\cdot)$ and $g_{LFV}(\cdot)$ according to equations (7), (8) and (11) respectively;
(V) Update the LSE equation shown in Eq. (18) using the morphological snakes scheme described in section IV. A;
(VI) Repeat the operations shown in steps (III) to (V) until the evolution process reaches the state of convergence.

process to noise and target edges, we make a certain tradeoff on all the test images and set it to 11. For the parameter c, which also comes from Eq. (8), since its function is only to prevent the coefficient from moving towards 0 prematurely, we empirically set it as 0.001 in this paper. In addition, for the parameters m and n from Eq. 7, since the evolution process is not very sensitive to its value, we empirically set it to the following values: $m = 1.5, n = 0.5$. The standard deviation σ of the Gaussian filter kernel shown in Eq. (14) will change from image to image, i.e., its value with a certain degree of image and task dependency. In addition, the time step Δt contained in the level set evolution process, the parameters μ and ε in Eq. (16) also vary with the changes of image data and segmentation tasks. For these task-related parameters, we will give their specific values in the caption position of the figures.

In the "Experimental results" sub-section, we will carry out detailed verification and testing from the following five aspects: quantitative evaluation of segmentation accuracy, rapidity caused by morphological snakes scheme, robustness against noise interference, adaptability to weak target edges and comparison with deep learning-driven CRF-RNN model [30]. Each of them corresponds exactly to an analysis or verification dimension of the proposed method. What needs to be emphasized here is that in order to test the wide adaptability of the proposed method to different kinds of image data, we select our test images from different data sources. One part of the data comes from the literature that has been published in the direction of image segmentation, and the other part comes from the Internet. In a word, these data are relatively independent, and the correlation between them is very weak. When initializing the evolution process of the LSF, we uniformly adopt the automatic initialization mechanism described in section IV. B. When setting up the family of comparison methods, we divide them into two categories: the first category is the level set segmentation models of non-deep learning type, and the second class is the semantic segmentation model of deep learning type. The first category includes the following five models: DRLSE model, LGDF model, LIF model, LPFE model and RSF-LoG model. The five comparison models are all representative and classical methods in the field of LSM. They are all data-driven type and do not contain any prior constraints, and the DRLSE model is the basis and starting point of the model framework of the proposed method. In conclusion, it is reasonable and scientific to use these methods as the family of comparison methods in this paper. We choose only one method for the second category, which is a well-known model called CRF-RNN [30] in the field of semantic segmentation. In order to highlight the uniqueness of this group of comparison experiments, we deliberately put it in a separate sub-section. In addition, when the task module needs to objectively measure the accuracy of the segmentation results, the metrics system shown in TABLE 1 can be adopted, where the range of the values of DSC, UDE, ODE, LE and F1-Score is $[0, 1]$, and the value range of MCC is $[-1, 1]$. Obviously, the closer of the values of DSC, F1-Score and MCC to 1, and the values of UDE, ODE and LE to 0, the better the segmentation results. In addition, the regional units represented by TP (true positives), FP (false positives),

TABLE 1. Metrics for evaluating the performance of segmentation algorithms.

Metrics	Description
DSC	The dice similarity coefficient (DSC) is used to compare the similarity between the segmented image and the reference image, which can be expressed in terms of true positives (TP), false positives (FP) and false negatives (FN) as: $Dice = 2TP/(2TP + FP + FN)$
UDE	The under-detection error (UDE) corresponds to those pixels in the reference contour that are not correctly segmented. Its definition is as follows: $UDE = FP/(FP + TN)$, where TN is true negatives.
ODE	The over-detection error (ODE) is used to measure the pixels in the detected contour that are not consistent with the reference contour, Its definition is as follows: $ODE = FN/(FN + TP)$.
LE	The localization error (LE) measures the distance between the misclassified pixels and the nearest pixels of the reference contour. LE is defined as follows: $LE = (FN + FP)/(TP + TN + FP + FN)$
F1-Score	The F1 score measures how close the predicted boundary of an object matches the ground truth boundary, and the F1-Score is defined as the harmonic mean of the precision and recall values with a distance error tolerance to decide whether a point on the predicted boundary has a match on the ground truth boundary or not: $F1\text{-}Score = 2 \times \mathrm{Precision} \times \mathrm{Recall}/(\mathrm{Precision} + \mathrm{Recall}) = 2TP/(2TP + FP + FN)$
MCC	The Matthews correlation coefficient (MCC) is used in machine learning as a measure of the quality of binary (two-class) classifications. The MCC is in essence a correlation coefficient between the observed and predicted binary classifications; it returns a value between −1 and 1. A coefficient of 1 represents a perfect prediction, 0 no better than random prediction and −1 indicates total disagreement between prediction and observation. MCC is defined as follows: $MCC = \frac{TP \times TN - FP \times FN}{\sqrt{(TP + FP)(TP + FN)(TN + FP)(TN + FN)}}$

FN (false negatives) and TN (true negatives) in TABLE 1 are shown in FIGURE 3.

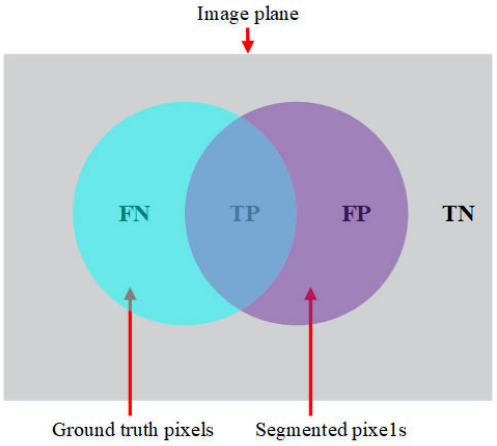

FIGURE 3. The geometric meanings of TP, FP, FN and TN in TABLE 1.

In the "Discussions" sub-section, we will analyze in detail several factors that can have a key impact on segmentation performance from the following aspects: an easy way to initialize a LSF ϕ, the effect of parameter ε on segmentation performance, the principles for selecting parameters μ and Δt and the application scenarios and limitations of the proposed method.

A. EXPERIMENTAL RESULTS

1) QUANTITATIVE EVALUATION OF SEGMENTATION ACCURACY

In this sub-section, we will use a set of experiments to quantitatively evaluate the accuracy of the segmentation results. The comparison methods used here are the five non-deep learning type models we mentioned in the guide part of the "EXPERIMENTAL RESULTS AND DISCUSSIONS" section. Specifically, they are the five models with abbreviations named DRLSE, LGDF, LIF, LPFE, and RSF-LoG. The first row of FIGURE 4 shows the original images along with initial contours, where the test images are a group of SAR images with river as the target of interest and obvious background interference, and the initial contours are derived from the proposed salient target detection mechanism-based automatic initialization process. The second to seventh rows are the segmentation results by using DRLSE, LGDF, LIF, LPFE, RSF-LoG and our EO-DRLSE models respectively. By carefully observing the comparison results shown in FIGURE 4, we can clearly see that the five comparison methods are all affected by background interference, and some (such as the fourth to fifth rows of the first column) even have a large number of background components in the final segmentation results. Since the proposed model adopts a set of efficient mechanisms to optimize the original DRLSE model, it outputs correct segmentation results on all four test images (as shown in the seventh row of FIGURE 4). TABLE 2 shows the segmentation metrics defined in TABLE 1 for the comparison experiments shown in FIGURE 4. It further

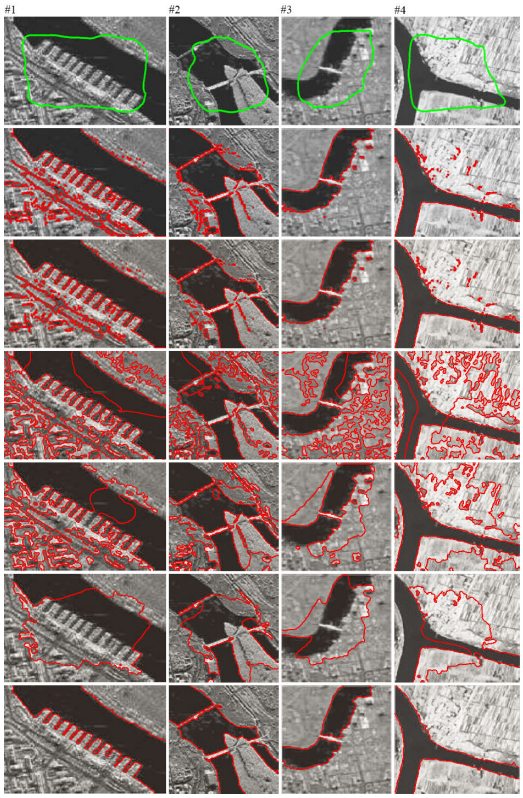

FIGURE 4. A set of comparison experiments used to rigorously verify the accuracy of the segmentation results. The first row shows the original images along with initial contours, and the second to the seventh rows are the segmentation results by using DRLSE, LGDF, LIF, LPFE, RSF-LoG and our EO-DRLSE models respectively. The relevant task parameters: $\mu = 0.04$, $\Delta t = 4.5$, $\sigma = 3$ and $\varepsilon = 3$.

confirms our observations from the objective data level: the proposed model achieves the optimal segmentation results both at the subjective and objective levels.

2) RAPIDITY CAUSED BY MORPHOLOGICAL SNAKES SCHEME

In this sub-section, we will quantitatively verify the rapidity of the evolution process caused by the morphological snakes scheme used in this paper, which is usually reflected by the number of iterations and the CPU time required to complete the entire evolution process. Here, we refer to number of iterations and CPU time collectively as convergence rate metrics. It is well known that the comparison of convergence rate metrics is meaningful only when the segmentation results of all the models participating in the comparison are correct. In view of this, in this group of comparison experiments, we turn off the salient target detection mechanism-based automatic initialization strategy and initialize the evolutionary process manually. At the same time, the optimal input parameters are adopted for each model involved in the comparison. The comparison methods used here are still the five non-deep learning type models we mentioned in the guide part of the "EXPERIMENTAL RESULTS AND DISCUSSIONS" section and we use a set of images with relatively homogeneous target regions and low background complexity.

TABLE 2. The segmentation metrics corresponding to the comparison experiments shown in figure 4.

Images	Methods	DSC	UDE	ODE	LE	F1-Score	MCC
#1	DRLSE	0.8944	0.1184	0.0053	0.0799	0.8944	0.8422
	LGDF	0.9126	0.0955	0.0054	0.0648	0.9126	0.8691
	LIF	0.3293	0.5025	0.6108	0.5394	0.3293	-0.1077
	LPFE	0.1832	0.4109	0.8188	0.5497	0.1832	-0.2310
	RSF-LoG	0.4261	0.4165	0.5105	0.4485	0.4261	0.0696
	EO-DRLSE	**0.9943**	**0.0023**	**0.0049**	**0.0039**	**0.9943**	**0.9914**
#2	DRLSE	0.9507	0.0504	0.0093	0.0360	0.9507	0.9243
	LGDF	0.9724	0.0254	0.0092	0.0197	0.9724	0.9575
	LIF	0.3993	0.4905	0.5236	0.5021	0.3993	-0.0135
	LPFE	0.0197	0.4119	0.9824	0.6117	0.0197	-0.4219
	RSF-LoG	0.3681	0.3386	0.6327	0.4416	0.3681	0.0287
	EO-DRLSE	**0.9872**	**0.0089**	**0.0091**	**0.0090**	**0.9872**	**0.9803**
#3	DRLSE	0.9807	0.0065	0.0139	0.0080	0.9807	0.9756
	LGDF	0.9839	0.0057	0.0107	0.0067	0.9839	0.9796
	LIF	0.4744	0.3678	0.2499	0.3434	0.4744	0.3113
	LPFE	0.0219	0.2811	0.9770	0.4248	0.0219	-0.2492
	RSF-LoG	0.5338	0.2482	0.2889	0.2566	0.5338	0.3945
	EO-DRLSE	**0.9893**	**0.0052**	**0.0101**	**0.0066**	**0.9893**	**0.9869**
#4	DRLSE	0.9714	0.0142	0.0126	0.0138	0.9714	0.9626
	LGDF	0.9737	0.0129	0.0119	0.0127	0.9737	0.9655
	LIF	0.3542	0.4564	0.4691	0.4594	0.3542	0.0635
	LPFE	0.0151	0.5522	0.9788	0.6534	0.0151	-0.4568
	RSF-LoG	0.2220	0.3826	0.7215	0.4630	0.2220	-0.0924
	EO-DRLSE	**0.9800**	**0.0052**	**0.0113**	**0.0095**	**0.9800**	**0.9738**

FIGURE 5 presents a set of comparison experiments for testing rapidity, where the first row shows the original images along with initial contours, and the second to the tenth rows are the segmentation results by using DRLSE, LGDF, LIF, LPFE, RSF-LoG and our EO-DRLSE models respectively. From the final convergence curves we can clearly see that all models output almost (there are only very small differences between the results) the same correct segmentation results. What needs to be specifically stated here is that the convergence state of this set of comparison experiments is very similar. Therefore, we have labeled the names of the algorithms on the final segmentation results so that they can be better visually distinguished. The corresponding convergence rate metrics for this set of experiments are shown in TABLE 3, and the sizes of these images are also shown under the image numbers. After analyzing the convergence rate metrics in TABLE 3, we find that our model achieves the best convergence performance because we adopt a morphological snake scheme that does not require solving complex partial differential equations. While the comparison methods all require a lot of time to solve the partial differential equations. Therefore, their number of iterations and CPU time are on the order of magnitude that is significantly different from the proposed scheme, namely, compared with the proposed scheme, their convergence efficiency is much lower.

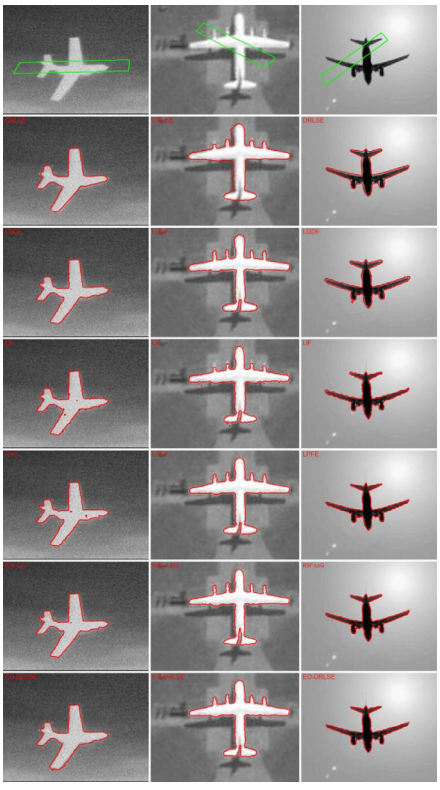

FIGURE 5. A set of comparison experiments for testing the rapidity of different methods. The first row shows the original images along with initial contours, and the second to the seventh rows are the segmentation results by using DRLSE, LGDF, LIF, LPFE, RSF-LoG and our EO-DRLSE models respectively. The relevant task parameters: $\mu = 0.06$, $\Delta t = 4.5$, $\sigma = 4.5$ and $\varepsilon = 2.5$.

TABLE 3. Comparison of convergence rate metrics for the images shown in the first row of figure 5 numbered from left to right. The description format of the metrics is: iteration number (CPU TIME (S)).

	image #1 (366×274)	image #2 (373×274)	image #3 (341×274)
DRLSE	150 (12.344)	167 (15.787)	141 (11.711)
LGDF	101 (9.985)	112 (11.115)	96 (9.511)
LIF	133 (18.953)	141 (20.119)	127 (18.187)
LPFE	91 (5.372)	104 (6.336)	87 (5.231)
RSF-LoG	127 (11.414)	138 (12.442)	115 (10.138)
EO-DRLSE	**8 (0.448)**	**11 (0.513)**	**6 (0.401)**

3) ROBUSTNESS AGAINST NOISE INTERFERENCE

The robustness here includes two aspects: one is the robustness to synthetic noise i.e., when we pollute a clean base image with external noise interference whose intensity can be accurately controlled, whether the algorithm can withstand the segmentation challenge caused by the increasing noise intensity; the other is the robustness to the imaging noise intrinsic in real-life images, i.e., when the input real-life image contains different degrees of background interference, can the algorithm suppress it and successfully extract the foreground target of the image?

FIGURE 6 shows a set of comparison experiments for the robustness to synthetic noise. In order to fully test the robustness to synthetic noise of the proposed method, we need a set of test images containing noise. The data generation strategy we adopted is as follows: firstly, a clean synthetic image is used as the basic image; then, additional noise interference (Gaussian noise) with increasing level is embedded in its data distribution. After the aforementioned noise mixing operation is completed, a set of test images with an accurately controlled degree of interference can be generated. The methods involved in this comparison are still the ones we used in FIGURE 5. The first row of FIGURE 6 is a sequence of test images superimposed with initial contours (provided by the automatic initialization mechanism described in section IV. B), and the control parameters ([mean, variance]) of the Gaussian noise corresponding to the second to fourth columns of FIGURE 6 are [0.05, 0.05], [0.1, 0.1], [0.15, 0.15]. The second to seventh rows are the segmentation results by using the DRLSE, LGDF, LIF, LPFE, RSF-LoG and our EO-DRLSE models respectively. Visually, we can see clearly that the five methods involved in the comparison only output the correct segmentation results on the basic image of this group of artificially noised data (the clean image without noise shown in the first column of FIGURE 6), while on the remaining images containing noise, they all output the wrong segmentation result, and the degree of segmentation error increases as the noise intensity increases. In sharp contrast, the proposed method outputs correct segmentation results on all four images (as shown in the last row of FIGURE 6).

FIGURE 7 shows another set of comparison experiments for this subsection, which focuses on the robustness of the algorithm to the imaging noise of real-life images, where the first row is the input images along with the output contours of the automatic initialization process. The comparison methods used in this group of experiments is the same as that in FIGURE 6. Since the proposed model does not contain any form of description and modeling unit for color features, we only consider the intensity information of the pixels. Therefore, when segmenting real-life images (color images), the input images actually involved in the operation are the gray versions of the real-life images. The first row of FIGURE 7 shows three real images from the BSDS500 dataset and the initial contours generated by the automatic initialization process. The second to seventh rows are the segmentation results by using the DRLSE, LGDF, LIF, LPFE, RSF-LoG and our EO-DRLSE models respectively. By visually observing these segmentation results, it is easy to know that the five methods involved in the comparison all output wrong segmentation results. What needs to be emphasized here is that in the case where our initialization curve does not include all the background information, these methods are still pulled to the wrong non-target position by the background interference. If all the background information is included in the initial curve, we have reason to believe that the error will be more serious at this time. On the contrary, our algorithm outputs correct segmentation results on all three images. Through the two sets of experiments shown in FIGURE 6 and FIGURE 7, we can draw the following conclusion: the functional components we constructed in sections III. C and III. D do provide a strong guarantee for the noise suppression ability (robustness to noise) of the proposed algorithm.

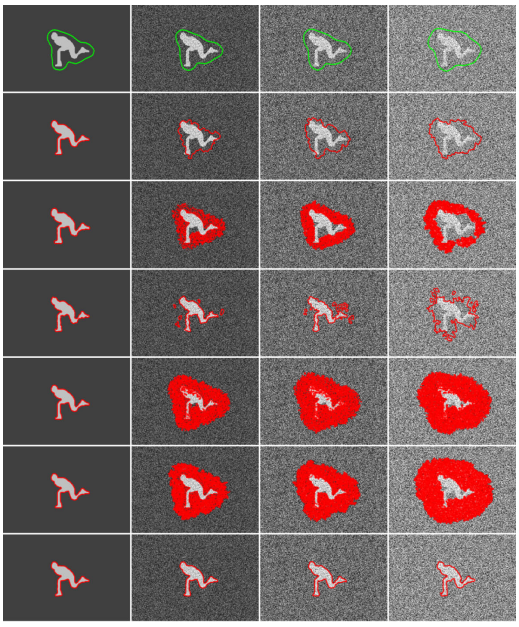

FIGURE 6. A set of comparison experiments for the robustness to synthetic noise. The first row is the input images containing initial contours. The second to seventh rows are the segmentation results by using the DRLSE, LGDF, LIF, LPFE, RSF-LoG and our EO-DRLSE models respectively, and the control parameters ([mean, variance]) of the Gaussian noise corresponding to the second to fourth columns are [0.05, 0.05], [0.1, 0.1], [0.15, 0.15], respectively. The relevant task parameters: $\mu = 0.02$, $\Delta t = 4.5$, $\sigma = 1.5$ and $\varepsilon = 4$.

4) ADAPTABILITY TO WEAK TARGET EDGES

In the previous model description chapter, we have argued that the proposed regularization term can make the evolution process not exceed the weak target edges, namely, our model has the guarantee of internal mechanism level in capturing weak target edges. In this section, we will validate the capability of the proposed model in terms of weak target edges capture through a set of comparison experiments. Here we use the same comparison methods system as FIGURE 7. We present this set of comparison experiments in FIGURE 8, where the first row is the input images (they are some typical

FIGURE 7. A set of comparison experiments for the robustness to the imaging noise of real-life images. The first row is the input images containing initial contours. The second to seventh rows are the segmentation results by using the DRLSE, LGDF, LIF, LPFE, RSF-LoG and our EO-DRLSE models respectively. The relevant task parameters: $\mu = 0.07$, $\Delta t = 4.5$, $\sigma = 5.5$ and $\varepsilon = 3.5$.

images with weak target edges) with the initial contours superimposed, and the second to seventh rows are the segmentation results by using the DRLSE, LGDF, LIF, LPFE, RSF-LoG and our SP-LEM models respectively. By carefully observing the segmentation results of the second to sixth rows of FIGURE 8, we find some obvious phenomena as follows: some of them stopped evolution prematurely, for example, the first column of the fifth to sixth rows; some of them went beyond the limit and crossed the real target boundary, for example, the third column of the second row; some of them were pulled to the wrong non-target location by background interference, for example, the second to fourth columns of the fourth row. In a word, the five methods involved in the comparison have different degrees of segmentation errors, which are caused by the internal mechanisms of the models themselves. Because the proposed model contains a mechanism that can effectively capture the of weak target edges, it outputs correct segmentation results (as shown in the seventh row of FIGURE 8) on all four test images.

5) COMPARISON WITH DEEP LEARNING-DRIVEN CRF-RNN MODEL

In recent years, the deep learning-based segmentation method has achieved fruitful results. It has become a mainstream and

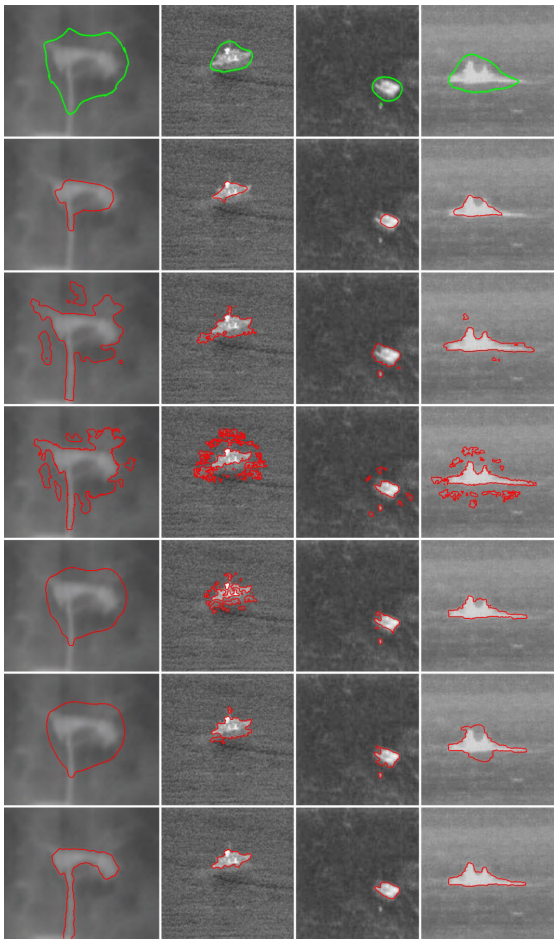

FIGURE 8. A set of comparison experiments for the adaptability to weak target edges. The first row is the input images containing initial contours. The second to seventh rows are the segmentation results by using the DRLSE, LGDF, LIF, LPFE, RSF-LoG and our EO-DRLSE models respectively. The relevant task parameters: $\mu = 0.02$, $\Delta t = 4.5$, $\sigma = 1.5$ and $\varepsilon = 3.5$.

standard image segmentation method in the case where large-scale image annotation data sets are available. In this section, we compare the proposed algorithm with the representative CRF-RNN model [30] in the semantic segmentation field through a set of experiments. Our annotation data set consists of 100 images. We use 80 of them as training images and the remaining 20 as test images. FIGURE 9 shows the comparison results of the two methods, where the first row is the test images superimposed with initial contours (required for the proposed level set segmentation model), and the second to third rows are the segmentation results of the CRF-RNN and our EO-DRLSE models respectively. In order to be consistent with the conventional expression of the semantic segmentation application, we also use the form of binary image to represent the segmentation results of our method. Visually, we can clearly see that the proposed method outputs completely correct segmentation results (as shown in the third row of FIGURE 9), while the segmentation results of CRF-RNN model have different degrees of errors (as shown in the second row of FIGURE 9). For example, the segmentation results show a significant target fracture

FIGURE 9. Comparison of segmentation results between our method and CRF-RNN model. The first row is the test images superimposed with initial contours, and the second to third rows are the segmentation results of the CRF-RNN and our EO-DRLSE models respectively. The relevant task parameters: $\mu = 0.07$, $\Delta t = 4.5$, $\sigma = 4.5$ and $\varepsilon = 3.5$.

TABLE 4. The segmentation metrics corresponding to the comparison experiments shown in figure 9 with the images numbered from left to right.

Images	Methods	DSC	UDE	ODE	LE	F1-Score	MCC
#1	CRF-RNN	0.9265	0.0037	0.0083	0.0038	0.9265	0.9267
	EO-DRLSE	**0.9766**	**0.0005**	**0.0076**	**0.0011**	**0.9766**	**0.9760**
#2	CRF-RNN	0.9223	0.0125	0.0069	0.0121	0.9223	0.9185
	EO-DRLSE	**0.9864**	**0.0002**	**0.0042**	**0.0020**	**0.9864**	**0.9854**
#3	CRF-RNN	0.7588	0.0130	0.3863	0.0040	0.7588	0.7794
	EO-DRLSE	**0.9828**	**0.0029**	**0.0310**	**0.0003**	**0.9828**	**0.9827**
#4	CRF-RNN	0.7600	0.0011	0.3855	0.0072	0.7600	0.7793
	EO-DRLSE	**0.9823**	**0.0002**	**0.0265**	**0.0007**	**0.9823**	**0.9821**

phenomenon accompanied by a large amount of scatter-like noise. We believe that there are two reasons for the segmentation errors of CRF-RNN model. One is from the annotation data level, specifically: since the dataset on which this group of experiments relies is very small, thus the segmentation model has not been fully trained, and it is reasonable that the segmentation ability is not strong. When the training data set becomes larger, we have reason to believe that its segmentation results will become more accurate. In other words, since it is a supervised deep learning algorithm, it is naturally dependent on the total amount of the annotated data. The other one is from the internal execution mechanism level of the sematic segmentation model, specifically: since CRF-RNN poses segmentation as a region-based pixel labeling, it cannot explicitly model the high-level dependencies between the points on the object boundary to preserve its overall shape, smoothness or the regional homogeneity within and outside the boundary. On the contrary, the proposed model is an unsupervised segmentation method, thus its segmentation result is only related to the performance of the model itself, and has no direct relationship with the amount of the input data. In TABLE 4, we give the accurate segmentation metrics (defined in TABLE 1) of this set of comparison experiments with similar segmentation results. These data, from a quantitative perspective, further confirm the superiority of the proposed algorithm.

B. DISCUSSIONS

1) AN EASY WAY TO INITIALIZE A LSF ϕ

Under the proposed combined regularization strategy, not only the time-consuming re-initialization operation required by the traditional level set method is completely eliminated, but also the level set function is no longer required to be initialized as a signed distance function. Our simple initialization method is as follows:

$$\phi_{initial}(x,y) = \begin{cases} -p, (x,y) \in \Omega_{initial} - \partial\Omega_{initial} \\ 0, (x,y) \in \partial\Omega_{initial} \\ p, (x,y) \in \Omega - \Omega_{initial} \end{cases} \quad (19)$$

where $\partial\Omega_{initial}$ is a set of pixels on the boundary of region $\Omega_{initial}$ enclosed by the initial contour (manually set or generated by some automatic segmentation algorithms), p is a positive constant and its selection rule is $p > 2\varepsilon$, where ε is the attribute parameter in Eq. (17).

Obviously, the initial level set function generated by the proposed initialization strategy shown in Eq. (19) is not a strictly signed distance function. During the evolution, although the level set function may not be able to maintain an approximate signed distance function at all pixel positions, the task flow can ensure that the evolution function remains an approximate signed distance function near the zero level set under the proposed regularization schemes shown in the first combined term of Eq. (16). Through a large number of experiments, we find that as long as the aforementioned conditions can be satisfied, the stability of the evolution process can be guaranteed.

2) THE EFFECT OF PARAMETER ε ON SEGMENTATION PERFORMANCE

The parameter ε in Eq. (17) has a direct impact on the curve capture range and the segmentation accuracy of the proposed model. The specific rules are as follows: the profile of function $\delta_\varepsilon^{new}(\phi)$ will vary with the value of parameter ε, and a bigger ε will cause a broader profile, which will expand the coverage of the evolution process but decrease the overall accuracy of the segmentation result. The relationship curve between function $\delta_\varepsilon^{new}(x)$ and independent variable x shown in FIGURE 10 further confirms the aforementioned influence rule in graphical form, i.e., the span (it is directly related to the coverage of the evolution process.) of function $\delta_\varepsilon^{new}(x)$ on the horizontal axis. Conversely, the sharpness (it directly affects the target positioning accuracy of the evolution curve) and peak value of the curve decrease as the parameter ε increases.

FIGURE 11 illustrates a set of verification experiments for testing the effect of parameter ε on the segmentation results. The test image used contains a small amount of Gaussian noise and a certain number of deeply concave regions (as shown in the first column of FIGURE 11). Here, we use a

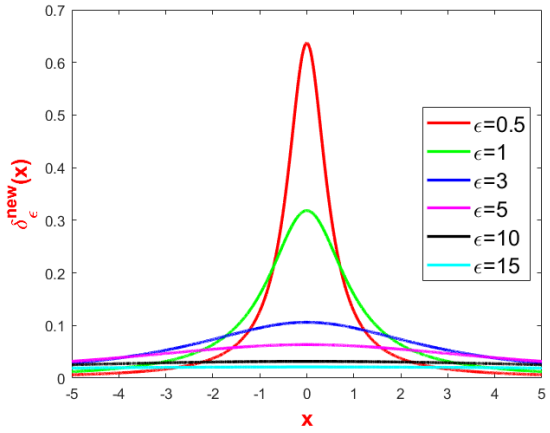

FIGURE 10. The relationship curve between function $\delta_\varepsilon^{new}(x)$ and independent variable x under different parameter ε.

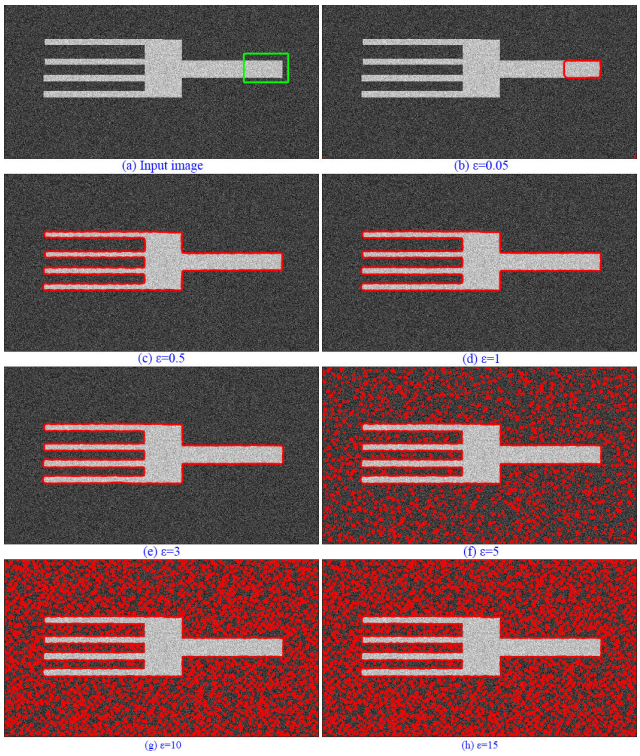

FIGURE 11. A set of verification experiments for testing the effect of parameter ε on the segmentation results The relevant task parameters: $\mu = 0.03$, $\Delta t = 6.5$ and $\sigma = 2.5$.

set of gradually increasing parameters ε whose set of values is $\{0.05, 0.5, 1, 3, 5, 10, 15\}$ to segment it. When the parameter ε is greater than or equal to 5 (corresponding to (f)-(h) of FIGURE 11), the coverage of the evolution process is indeed extended to a very large image range, and the deep recessed region components are successfully segmented. However, the interference effect of background clutter on segmentation process becomes very obvious, and the degree of interference becomes stronger and stronger with the increase of parameter ε. On the contrary, when parameter ε is very small (corresponding to (b) of FIGURE 11), the behavior of the curve will become extremely localized, and the evolution curve cannot be pushed into the deep depression concave regions, namely, under such parameter configuration, the evolution process cannot be effectively expanded, in other word, this is equivalent to the other extreme of positioning behavior. What needs to be specifically explained here is that in FIGURE 10, we do not shown the relationship curve when the parameter ε has a value of 0.05 (corresponding to (b) of FIGURE 11). The main reason is that under such an extremely small parameter ε, the top shape of the curve will become extremely steep, and the other curves will be pressed very low. Obviously, this is very unfavorable for the display of comparison effect, so we omitted it.

Based on our analytical experiments, we can easily derive the following parameter selection principles: when parameter ε is taken in range $[0.5, 3]$, a good compromise between capture range and location accuracy can be achieved.

3) THE PRINCIPLES FOR SELECTING PARAMETERS μ AND Δt

In the numerical implementation stage, the time step Δt can be much larger than that of the parameter that plays the same role in the traditional LSMs. Under the premise of ensuring positioning accuracy and evolution speed, we try to choose Δt within a relatively large span. For example, from 0.15 to 120. Now, naturally, a question arises: what is the value range of Δt in which the LSE process does not cause oscillation? Through a large number of validation experiments, we have found that as long as the coupling relationship between μ and Δt satisfies $\mu \Delta t < 0.25$, the evolution process can be guaranteed to be stable. By increasing the time step Δt, we can indeed speed up the evolution process. However, when its value is too large, there is a great possibility that serious positioning errors and oscillations will occur. Therefore, we need to make a reasonable compromise between the time step, the positioning accuracy and the stability of evolution process. For most test images, our selection range for Δt is $\Delta t \leq 12.5$.

4) THE APPLICATION SCENARIOS AND LIMITATIONS OF THE PROPOSED METHOD

In the five verification dimensions of the experimental results sub-section, the comprehensive performance of the proposed method is very excellent. However, in the field of image segmentation, there are two typical types of images, namely, the texture images with high repetition rate of feature patterns and the inhomogeneous images with strong inhomogeneity. We did not conduct targeted experiments on these two types of data. In this sub-section, we will further verify the data adaptability of our method through a set of segmentation experiments for special images. The first row of FIGURE 12 shows the test images along with initial contours (set manually), where the test data set consists of two texture images with very distinct pattern features and two inhomogeneous images with obvious inhomogeneity in target region, and the second row shows the segmentation results of the proposed method. From this set of segmentation results, we can

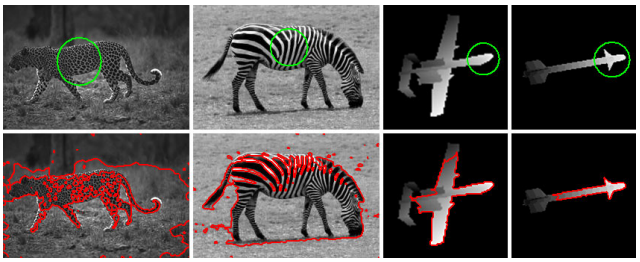

FIGURE 12. A set of validation experiments for texture images and non-homogeneous images. The relevant task parameters: $\mu = 0.03$, $\Delta t = 8$, $\sigma = 2.5$ and $\varepsilon = 3.5$.

clearly see that for texture-type images, the proposed method is powerless because it does not contain any processing units that can effectively express the texture components. At the same time, the performance of the model is not good enough in the segmentation task of inhomogeneous images. The reason is that we do not deliberately model the local features of the image and embed it as an independent energy component into the total energy functional. In summary, we can summarize the application scenarios and limitations of the proposed method as follows: our method is especially suitable for segmenting noise and weak edge images whose inhomogeneity in target region is not very strong. For texture images with very obvious pattern features and inhomogeneous images with strong inhomogeneity, the proposed method can only give ordinary level segmentation results.

VI. CONCLUSION

In this paper, the mechanism defects of the original DRLSE model are deeply improved and optimized from various aspects. Our model has shown excellent performance in terms of accuracy of segmentation results, rapidity of evolution process, robustness against noise, adaptability to weak target edges. We will provide a detailed summary of each of the elements that have been optimized and improved, and point out the future research and development directions.

The specific optimization elements are as follows: (1) based on the local normalized entropy and local fitting means of the image, we construct two adaptive coefficients, one of which is the coefficient λ_{length} corresponding to the length regularization term. Its value changes adaptively with the change of image disturbance characteristics (which can be described by local entropy), and the degree of regularization can be adjusted dynamically. The other is the coefficient ν_{LFM} corresponding to the regional term, whose adaptive characteristic makes the advancing speed of evolution process can be adjusted dynamically with the change of local fitting means; (2) based on the local fitting variances, we construct an improved edge stop function, which enables the evolution process to maintain a considerable evolution speed in the non-target noise interference position without stopping. Obviously, this gives our algorithm a particularly strong noise suppression ability; (3) an adaptive regularization term which specially serves for the zero level set is constructed, which forms a strong extension to the level set regularization scheme of the original DRLSE model; (4) in order to overcome the inherent structural defects of the traditional finite difference scheme and improve the automation of the initialization process, in the implementation stage, we adopt two sets of strategies. One is a fast numerical solution based on morphological snakes, which replaces the floating point differential operations required by the traditional partial differential equations by means of special integer morphological operations. The other is an automatic initialization scheme based on salient target detection mechanism, which makes the proposed algorithm fully automated. This kind of processing is extremely valuable in some applications where human participation is not allowed.

In future research, we will continue to develop high-performance segmentation models and adopt more efficient numerical strategies to solve them. At the same time, in order to meet the challenges from visual big data, we will follow the ideas constructed in references [31] and [32] to further accelerate the computing process within the framework of parallel processing.

ACKNOWLEDGMENT

The authors would like to thank the anonymous reviewers for their valuable comments and advices.

REFERENCES

[1] X. Chen, F. He, and H. Yu, "A matting method based on full feature coverage," *Multimedia Tools Appl.*, vol. 78, no. 9, pp. 11173–11201, May 2019.
[2] S. Osher and J. A. Sethian, "Fronts propagating with curvature-dependent speed: Algorithms based on Hamilton-Jacobi formulations," *J. Comput. Phys.*, vol. 79, no. 1, pp. 12–49, 1988.
[3] V. Caselles, R. Kimmel, and G. Sapiro, "Geodesic active contours," *Int. J. Comput. Vis.*, vol. 22, no. 1, pp. 61–79, 1997.
[4] C. Li, C. Xu, C. Gui, and M. D. Fox, "Distance regularized level set evolution and its application to image segmentation," *IEEE Trans. Image Process.*, vol. 19, no. 12, pp. 3243–3254, Dec. 2010.
[5] X. Gao, B. Wang, D. Tao, and X. Li, "A relay level set method for automatic image segmentation," *IEEE Trans. Syst., Man, Cybern. B, Cybern.*, vol. 41, no. 2, pp. 518–525, Apr. 2011.
[6] S. Zhu and R. Gao, "A novel generalized gradient vector flow snake model using minimal surface and component-normalized method for medical image segmentation," *Biomed. Signal Process. Control*, vol. 26, pp. 1–10, Apr. 2016.
[7] Y. Wu, Y. Wang, and Y. Jia, "Adaptive diffusion flow active contours for image segmentation," *Comput. Vis. Image Understand.*, vol. 117, no. 10, pp. 1421–1435, 2013.
[8] Y. Wu, Y. Wang, and Y. Jia, "Segmentation of the left ventricle in cardiac cine MRI using a shape-constrained snake model," *Comput. Vis. Image Understand.*, vol. 117, no. 9, pp. 990–1003, 2013.
[9] S. Zhou, B. Li, Y. Wang, C. Wang, T. Wen, and N. Li, "The line- and block-like structures extraction via ingenious snake," *Pattern Recognit. Lett.*, vol. 112, pp. 324–331, Sep. 2018.
[10] H. Yu, F. He, and Y. Pan, "A novel segmentation model for medical images with intensity inhomogeneity based on adaptive perturbation," *Multimedia Tools Appl.*, vol. 78, no. 9, pp. 11779–11798, 2019.
[11] T. F. Chan and L. A. Vese, "Active contours without edges," *IEEE Trans. Image Process.*, vol. 10, no. 2, pp. 266–277, Feb. 2001.
[12] S. Niu, Q. Chen, L. de Sisternes, Z. Ji, Z. Zhou, and D. L. Rubin, "Robust noise region-based active contour model via local similarity factor for image segmentation," *Pattern Recognit.*, vol. 61, pp. 104–119, Jan. 2017.
[13] L. Liu, D. Cheng, F. Tian, D. Shi, and R. Wu, "Active contour driven by multi-scale local binary fitting and Kullback-Leibler divergence for image segmentation," *Multimedia Tools Appl.*, vol. 76, no. 7, pp. 10149–10168, 2017.

[14] C. Li, C.-Y. Kao, J. C. Gore, and Z. Ding, "Minimization of region-scalable fitting energy for image segmentation," *IEEE Trans. Image Process.*, vol. 17, no. 10, pp. 1940–1949, Oct. 2008.
[15] L. Wang, L. He, A. Mishra, and C. Li, "Active contours driven by local Gaussian distribution fitting energy," *Signal Process.*, vol. 89, no. 12, pp. 2435–2447, Dec. 2009.
[16] K. Zhang, H. Song, and L. Zhang, "Active contours driven by local image fitting energy," *Pattern Recognit.*, vol. 43, no. 4, pp. 1199–1206, Apr. 2010.
[17] K. Ding, L. Xiao, and G. Weng, "Active contours driven by region-scalable fitting and optimized Laplacian of Gaussian energy for image segmentation," *Signal Process.*, vol. 134, pp. 224–233, May 2017.
[18] K. Ding, L. Xiao, and G. Weng, "Active contours driven by local pre-fitting energy for fast image segmentation," *Pattern Recogn. Lett.*, vol. 104, no. 1, pp. 29–36, Mar. 2018.
[19] H. Yu, F. He, and Y. Pan, "A novel region-based active contour model via local patch similarity measure for image segmentation," *Multimedia Tools Appl.*, vol. 77, no. 18, pp. 24097–24119, Sep. 2018.
[20] P. Marquez-Neila, L. Baumela, and L. Alvarez, "A morphological approach to curvature-based evolution of curves and surfaces," *IEEE Trans. Pattern Anal. Mach. Intell.*, vol. 36, no. 1, pp. 2–17, Jan. 2014.
[21] B. Zhou and C.-L. Mu, "Level set evolution for boundary extraction based on a p-Laplace equation," *Appl. Math. Model.*, vol. 34, no. 12, pp. 3910–3916, 2010.
[22] D. Wang, T. Zhang, W. Shi, Z. Wang, X. Yang, and L. Wei, "Moving objects segmentation based on piecewise constant Mumford-Shah model solving by additive operator splitting," *Opt. Eng.*, vol. 49, no. 3, 2010, Art. no. 037004.
[23] D. Wang, "Hybrid fitting energy-based fast level set model for image segmentation solving by algebraic multigrid and sparse field method," *IET Image Process.*, vol. 12, no. 4, pp. 539–545, 2018.
[24] D. Wang, "A fast hybrid level set model for image segmentation using lattice Boltzmann method and sparse field constraint," *Int. J. Pattern Recognit. Artif. Intell.*, vol. 32, no. 6, 2018, Art. no. 1854015.
[25] S. Goferman, L. Zelnik-Manor, and A. Tal, "Context-aware saliency detection," *IEEE Trans. Pattern Anal. Mach. Intell.*, vol. 34, no. 10, pp. 1915–1926, Oct. 2012.
[26] E. Erdem and A. Erdem, "Visual saliency estimation by nonlinearly integrating features using region covariances," *J. Vis.*, vol. 13, no. 4, pp. 1–20, Mar. 2013.
[27] R. Achanta, S. Hemami, F. Estrada, and S. Susstrunk, "Frequency-tuned salient region detection," in *Proc. IEEE Conf. CVPR*, Jun. 2009, pp. 1597–1604.
[28] J. Harel, C. Koch, and P. Perona, "Graph-based visual saliency," in *Proc. Adv. Neural Inf. Process. Syst.*, vol. 19, 2007, pp. 545–552.
[29] X. Hou and L. Zhang, "Saliency detection: A spectral residual approach," in *Proc. IEEE Conf. CVPR*, Jun. 2007, pp. 1–8.
[30] S. Zheng, S. Jayasumana, B. Romera-Paredes, V. Vineet, Z. Su, D. Du, C. Huang, and P. H. S. Torr, "Conditional random fields as recurrent neural networks," in *Proc. IEEE Int. Conf. Comput. Vis.*, Dec. 2015, pp. 1529–1537.
[31] Y. Zhang, F.-Z. He, N. Hou, and Y. M. Qiu, "Parallel ant colony optimization on multi-core SIMD CPUs," *Future Gener. Comput. Syst.*, vol. 79, pp. 473–487, May 2018.
[32] Y. Zhou, F. He, and Y. Qiu, "Dynamic strategy based parallel ant colony optimization on GPUs for TSPs," *Sci. China Inf. Sci.*, vol. 60, no. 6, 2017, Art. no. 068102.

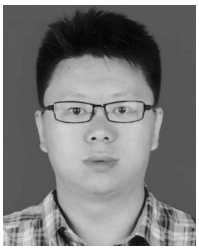

DENGWEI WANG received the B.S. degree in automation from the Wuhan University of Science and Technology, Wuhan, China, in 2005, and the M.S. degree in control theory and control engineering and the Ph.D. degree in control science and engineering from the Huazhong University of Science and Technology, Wuhan, in 2007 and 2011, respectively. From September 2011 to October 2014, he was with the Key Laboratory of Electronic Information and Control, Southwest China Research Institute of Electronic Equipment. He is currently a Lecturer with the School of Aeronautics and Astronautics, University of Electronic Science and Technology of China. His research interests include visual target detection and recognition, image segmentation, deep learning, and level set methods.